Supplementary Information: Twist angle dependent interlayer transfer of valley polarization from excitons to free charge carriers in WSe$_2$/MoSe$_2$ heterobilayers

Frank Volmer[1,2], Manfred Ersfeld[1], Paulo E. Faria Junior[3],
Lutz Waldecker[1,4], Bharti Parashar[5], Lars Rathmann[1],
Sudipta Dubey[1], Iulia Cojocariu[5], Vitaliy Feyer[5,6],
Kenji Watanabe[7], Takashi Taniguchi[8], Claus M. Schneider[5,6],
Lukasz Plucinski[5], Christoph Stampfer[1,9], Jaroslav Fabian[3],
Bernd Beschoten[1,10]

[1]2nd Institute of Physics and JARA-FIT, RWTH Aachen University,
52074 Aachen, Germany.
[2]AMO GmbH, Advanced Microelectronic Center Aachen (AMICA),
52074 Aachen, Germany.
[3]Institut für Theoretische Physik, Universität Regensburg, D-93040
Regensburg, Germany.
[4]Department of Applied Physics, Stanford University, 348 Via Pueblo
Mall, Stanford, CA 94305, USA.
[5]Peter Grünberg Institute (PGI-6), Forschungszentrum Jülich GmbH,
52428 Jülich, Germany.
[6]Fakultät für Physik and Center for Nanointegration Duisburg-Essen
(CENIDE), Universität Duisburg-Essen, D-47048 Duisburg, Germany.
[7]Research Center for Functional Materials, National Institute for
Materials Science, Tsukuba 305-0044, Japan.
[8]International Center for Materials Nanoarchitectonics, National
Institute for Materials Science, Tsukuba 305-0044, Japan.
[9]Peter Grünberg Institute (PGI-9), Forschungszentrum Jülich, 52425
Jülich, Germany.
[10]JARA-FIT Institute for Quantum Information, Forschungszentrum
Jülich GmbH and RWTH Aachen University, 52074 Aachen, Germany.

Supplementary Note 1: Second Harmonic Generation

The twist angles in the heterobilayer devices were determined by measurements of the polarization dependence of the second harmonic (SH) generation intensity. In monolayer samples, this dependence immediately indicates the orientation of the crystallographic axes [1, 2]. In a heterobilayer, the SH field is given by a vector superposition of the individual SH fields of both monolayers, which allows to distinguish natural stacking with almost complete destructive interference from the unnatural stacking with constructive interference [3].

We measured the SH intensity on parts of isolated monolayers of both materials as well as on the bilayer part. Supplementary Figure 1 shows a representative measurement of the intensities of the SH emission as a function of the azimuthal angle of the linearly polarized incident laser in case of LTA device #1 of the main manuscript. The data of the monolayers was fitted with the function $I_\Theta = I_0 \cdot \sin^2(3\Theta)$. The difference of the numerically optimized angles Θ between the different areas is the relative twist angle given in the main manuscript. In the case of small angles between the crystallographic axes (STA devices #1 and #2), the SH intensity of the bilayer was compared to the intensity of both monolayers, which identifies the twist angle of STA device #1 as $7°$ and of STA device #2 as $56°$, which is a small twist angle of $60° - 56° = 4°$ to an H-type stacking order.

Due to quite different sizes of the two TMD flakes in LTA device #3 and the use of the monolayer parts for electrical contacts, we were not able to obtain the necessary SHG measurements on the respective monolayer areas in this device. Therefore, we cannot give a twist angle for this device. However, we note that we intentionally misaligned the edges of the TMD flakes during the stacking process to achieve a large twist angle. The PL and TRKR measurements indicate that the large twist angle was indeed achieved.

The laser used in the experiments had a pulse duration of approximately $200\,\text{fs}$, a repetition rate of $100\,\text{MHz}$ and a central wavelength of $1030\,\text{nm}$. The average power used was between $20\,\text{mW}$ and $40\,\text{mW}$.

Supplementary Note 2: Sensitivity of Kerr signal to free charge carriers

As we have demonstrated in Ref. [4], time-resolved Kerr rotation is not only sensitive to valley-polarized excitons but can also detect a valley polarization of free charge carriers, if the energy of the probe pulse is tuned to the trion (charged exciton) energy of the corresponding TMD. This is due to the fact that both the helicity of the incoming light and its energy determines what type of trion (singlet or triplet) is formed and in which valley the trion is created [5–7]. As the formation of trions necessitates the presence of additional charge carriers [5], the free charge carrier density inside the valley directly impacts the probability with which photons with matching helicity and energy interact with the corresponding valley. The sensitivity of the linearly polarized probe pulse on a valley polarization can therefore be explained by the fact that the
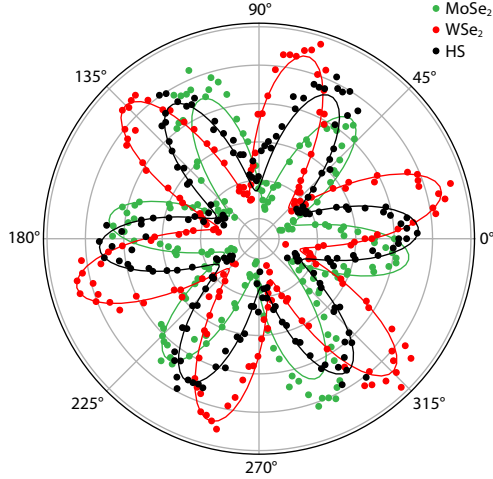
Supplementary Figure 1 Polar plot of the polarization-dependent second harmonic intensity as a function of the azimuthal angle of the linearly polarized incident laser for LTA device #1 of the main manuscript.

probe pulse is a superposition of left and right circularly polarized light, which have different probabilities to interact with the TMD in the presence of a valley polarization of free charge carriers. Of course, this is a simplified explanation as discussed in the next section.

Supplementary Note 3: No sensitivity of Kerr signal to interlayer excitons

Our observations in the main manuscript raise the question of why TRKR does not seem to be able to detect a polarization of interlayer excitons. The main problem in this respect is that it is everything but trivial to derive a theoretical expression for the expected Kerr signal. This is due to the fact that the devices in our study are complex multilayer structures that consist of magneto-optic materials (the TMDs) and dielectric materials (hBN and SiO_2) placed on a highly reflective substrate (Si). This greatly complicates the derivation of an expression for the Kerr signal, as discussed in Refs. [8–10]. To our knowledge, there is no theoretical derivation of the Kerr signal for TMD heterobilayers to date.

In the energy range of the interlayer exciton such a derivation might be especially difficult, as it was shown that interlayer excitons at different moiré sites can exhibit opposite optical selection rules [11–14]. Therefore, it is not clear if an interlayer exciton polarization can actually rotate the linear polarization of the probe pulse, i.e. creating a Kerr rotation.
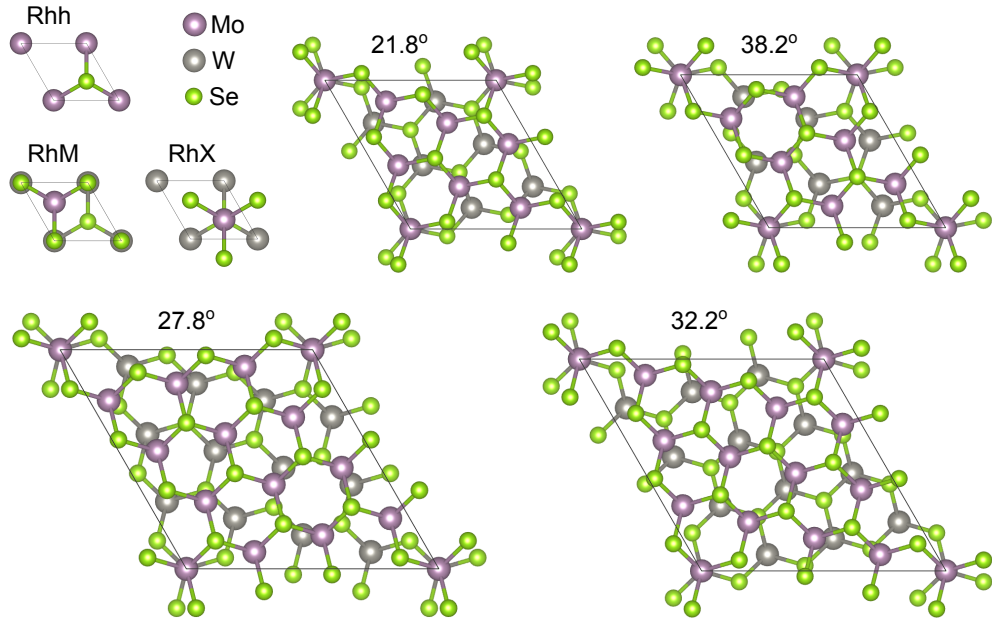
Supplementary Figure 2 Supercells for R-stacking and large twist angles investigated within first principles.

Supplementary Note 4: Band structure calculations

We performed the first principles calculations of the R-stacked (0° twist) and large twist angles (21.8°, 38.2°, 32.2° and 27.8°) $MoSe_2/WSe_2$ heterostructures based on the density functional theory using the all-electron full-potential linearized augmented plane-wave method implemented within the Wien2k package [15]. We used the Perdew–Burke–Ernzerhof [16] exchange-correlation functional with van der Waals interactions accounted via the D3 correction [17]. The wavefunction expansion into atomic spheres takes into account orbital quantum numbers up to 10 and the plane-wave cut-off multiplied with the smallest atomic radii is set to 7. Spin–orbit coupling was included fully relativistically for core electrons, while valence electrons were treated within a second-variational procedure [18] with the scalar-relativistic wavefunctions calculated in an energy window up to 2 Ry. Self-consistency was achieved using a two-dimensional Monkhorst–Pack k-grid with 12x12 (6x6) points for the R-stacked (twisted) structure and the convergence criteria of 10^{-5} e for the charge and 10^{-5} Ry for the energy was used. We built commensurate heterostructures with a common in-plane lattice parameter of 3.2855 $\mathring{A}$ for $MoSe_2$ and WSe_2 layers (as an average value of their individual lattice parameters [19]). This average lattice parameter leads to an effective strain of $\sim 0.1\%$ to the individual layers, which is sufficiently small to affect the energy- and spin- dependent properties [20, 21]. A vacuum region of 16 Å was assumed in all cases. We minimized the energy to find the equilibrium interlayer distances, obtaining 3.724 Å for the Rhh stacking, 3.074 Å for the RhM stacking, 3.084

4
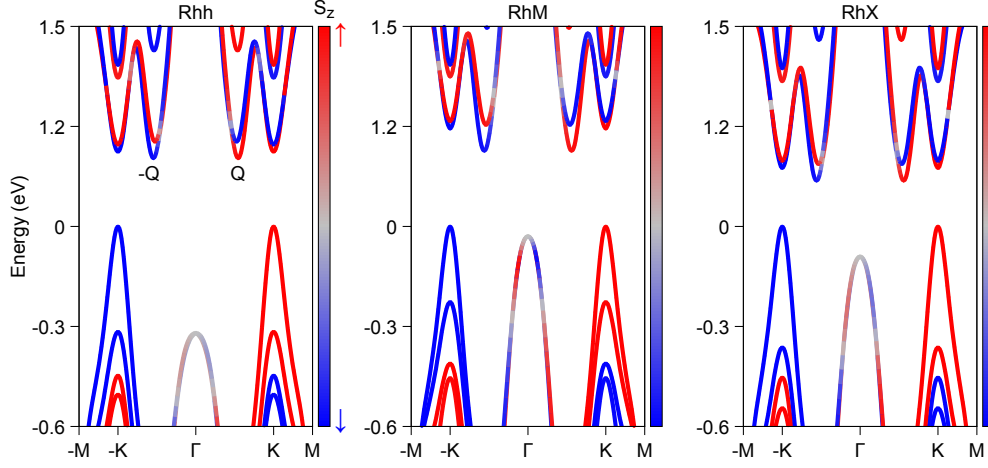
Supplementary Figure 3 Spin-resolved band structures for the three different R-type stackings at $0\,^\circ$ twist-angle.
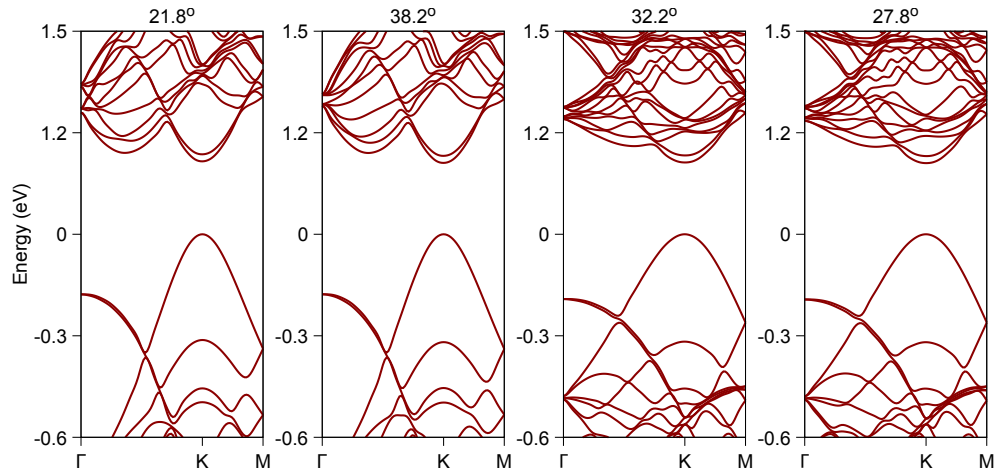
Supplementary Figure 4 Calculated band structures for large twist angles.

Å for the RhX stacking, 3.337 Å for the 21.8° and 38.2° twisted structures and 3.365 Å for the 32.2° and 27.8° twisted structures. In Supplementary Figure 2 we present the top view of each crystal structure considered in our study, namely, the Rhh, RhM and RhX stackings (0° twist angle) and the large twist angle cases 21.8°, 38.2°, 32.2° and 27.8°.

Supplementary Figure 3 shows the calculated band structures for the three different R-type stackings at $0\,^\circ$ twist-angle (see Supplementary Figure 2 for a description of these stacking orders). Depending on the type of stacking, the positions of the
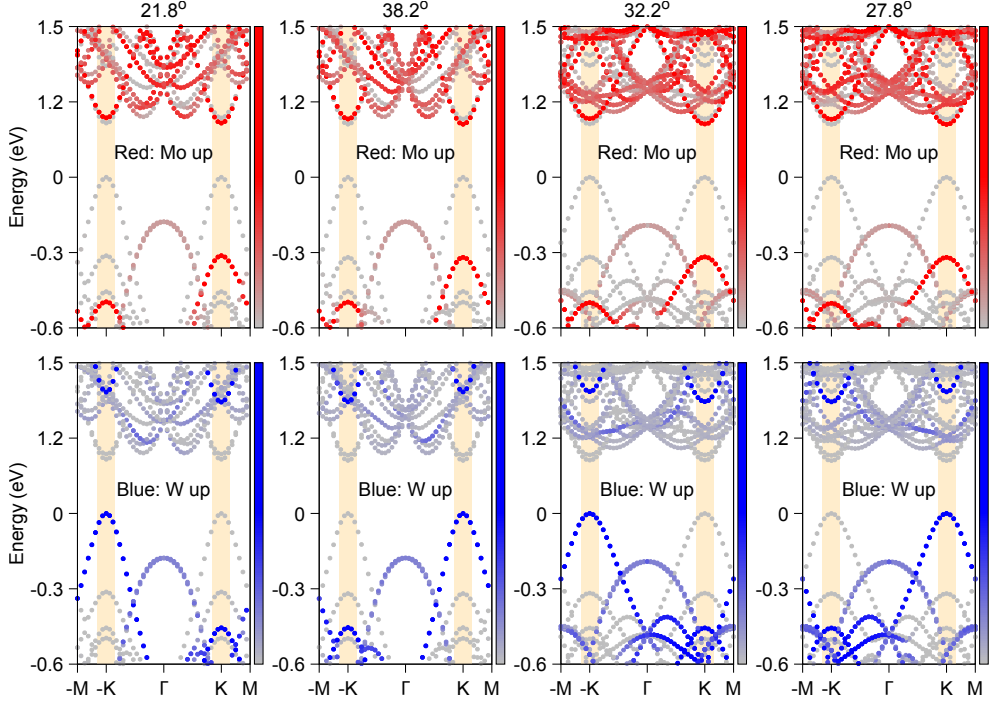
Supplementary Figure 5 Band structures for large twist angles with highlighted contributions from the spin-up states of molybdenum and tungsten atoms.

Γ- and Q-valleys can shift quite significantly with respect to the K-valleys. Furthermore, together with external parameters like interlayer distance [22] (which might be impacted by fabrication-induced contamination between the TMD layers) or strain [20], the difference in stacking order might be the reason that STA device #2 shows a less pronounced hybridization than STA device #1 despite its smaller twist-angle between the crystallographic axes. This is supported by a recent publication by some co-authors, in which the high-symmetry stackings (R- and H-type) are investigated under electric fields and varying interlayer distances [23]. In Figs. 1 and 2 of Ref. [23], R- and H-type stackings do show different energy alignments between K-, Γ-, and Q-bands, as well as different dependencies with respect to changes in the electric field and interlayer distance (see Figs. 3 and 7 of Ref. [23]).

The color-code in Supplementary Figure 3 depicts the spin-texture in the out-of-plane direction. Whereas the conduction band minimum at the Q-valley is showing a small spin-splitting, the valence band maximum at the Γ-valley is spin-degenerated, therefore likely enhancing spin-flip scattering in the valence band as described in the main manuscript.

Supplementary Figure 4 depicts the calculated band structures for the several large twist angles analyzed. We note that all of our calculations resulted in a type II band alignment, consistent with previous theoretical studies, but at odds with our

Supplementary Table 1 Dipole matrix elements, $|p_{cv}^{\epsilon}| = |\langle v, K | \hat{\epsilon} \cdot \vec{p} | c, K \rangle|$ (in eV.Å), and their respective polarization, $\epsilon = \{+, -, z\}$, calculated at the K-point of the studied systems.

	intralayer from VB+(Mo)		intralayer from VB+(W)		interlayer from VB+(W)	
	to CB-(Mo)	to CB+(Mo)	to CB-(W)	to CB+(W)	to CB-(Mo)	to CB+(Mo)
Rhh	4.62955, +	0.11176, z	0.36211, z	5.85025, +	0.32198, +	0.05107, z
RhM	4.56963, +	0.15023, z	0.23852, z	5.85374, +	0.36175, z	0.01253, -
RhX	4.64344, +	0.12416, z	0.41587, z	5.83282, +	0.28064, -	0.15099, +
21.8°	4.63933, +	0.12007, z	0.34812, z	5.79177, -	0.00146, z	0.01181, -
38.2°	4.65387, +	0.09271, z	0.30346, z	5.81078, +	0.02484, +	0.00277, z
32.2°	4.65803, +	0.09021, z	0.29798, z	5.84845, -	0.00004, z	0.00030, -
27.8°	4.65539, +	0.11436, z	0.25132, z	5.84818, +	0.00802, +	0.00028, z

experimental data. So far, theoretical studies only show a transition from a type II to a type I band alignment in case of large displacement fields [24, 25]. However, the necessary strength of the displacement field lies far beyond our applicable gate voltage range. Furthermore, in our devices we do not have the combination of both a bottom and a top gate, which is necessary to create a displacement field without simultaneously inducing charge carriers into the heterostructure [26].

On the other hand, there is one experimental study that argues to observe a transition from a type II to a type I band alignment in case of large charge carrier densities [27]. In this respect, we note that to our knowledge all previous band structure calculations of TMD heterostructures (including our own calculations) are done under the assumption of charge neutrality. This limitation is due to an increase in complexity of the models and especially a significant increase in required computational power if doping is also taken into account. Nonetheless, there has been theoretical efforts along this line but still restricted to monolayers [28, 29]. As most of our devices show a slight n-doping, we therefore propose that the unexpected band alignment, which is derived from our experimental data, might be caused by a combination of the large twist angle together with the presence of donor states in both TMD layers. It has to be the scope of further studies to investigate this idea further.

Our calculations can also shed some light on the observation that most WSe$_2$/MoSe$_2$-heterobilayers (especially the ones with small twist angle) show a stronger quenching of the WSe$_2$ intralayer exciton compared to the MoSe$_2$ intralayer exciton, as mentioned in the main manuscript. Table 1 contains calculated transition rates for neutral excitons at the K-point for the different R-stackings and large twist angles analyzed. Whereas the transition rate for the interlayer exciton significantly drops towards larger twist angles (explaining the vanishing of the interlayer exciton in PL measurements of devices with large twist-angle), the intralayer transitions are barely effected by the twist angle and are similar to the ones in the respective monolayer case. Most importantly, the two bright exciton transitions of WSe$_2$ [VB+(W)→CB+(W)] and MoSe$_2$ [VB+(Mo)→CB-(Mo)] have very comparable transition rates.

To understand the often missing WSe$_2$ exciton emission in heterobilayers, we now only have to take into consideration that the intensity of a PL signal depends on both

the transition rate and the occupation number in the respective states. As the transition rates are very comparable to each other, our calculations therefore suggest that photo-excited charge carriers must scatter quite fast away from either the valence band maximum or the upper, spin-split conduction band minimum of WSe_2. We assume that the upper, spin-split conduction band minimum is actually responsible for this effect. To support our assumption, we present in Supplementary Figure 5 the band structures of the large twist angle cases highlight the contributions of the spin-up states of each layer, denoted by the molybdenum and tungsten atoms. Spin-down states are just the time-reversal partners of spin-up states are are not show for simplicity.

We observe a magnitude of zone-folded bands near the conduction band minima of WSe_2. Because of these bands, we assume that photo-excited electrons quite efficiently scatter away from the conduction band K-valleys of WSe_2 and therefore are not available for the optical recombination process. On the other hand, at the K-valley both the valence and conduction bands of $MoSe_2$ are quite well-separated from other bands. Therefore, scattering might take longer, which in turn increases the chance of optical recombination, which makes the corresponding PL signal to a quite prominent one in our measurements.

Whereas these zone-folded bands can explain the significantly quenched PL emission from WSe_2 in heterostructures that exhibit the widely assumed type II band alignment, the quite strong PL emission from WSe_2 in both LTA devices #1 and #3 demonstrate that these devices do not possess these pronounced zone-folded bands near the conduction band minima of WSe_2. It must be the scope of further studies, if an alignment of the conduction band minima of WSe_2 and $MoSe_2$ caused by donor states (as derived in the main manuscript) has this effect.

Supplementary Note 5: Possible impact of a moiré potential

The sub-peaks seen in the interlayer exciton emission in Fig. 1d of the main manuscript were also previously attributed to the presence of a moiré potential [30–32]. Therefore, the question arises if a moiré superlattice and its associated potential may play a role in the observed valley and spin dynamics discussed in the main manuscript (we assume that the twist angles even for the STA devices are too large for atomic reconstruction [33, 34]). First, we note that a moiré potential might only be relevant for the STA devices, as the large twist angles in the LTA devices result in moiré periods that are most likely too small to be able to form a moiré potential that can trap charges [30]. Instead, for small twist angles it was shown that the resulting moiré potentials can lead to a spatial trapping of charge carriers [31, 35, 36]. However, the associated moiré excitons can exhibit lifetimes of up to hundreds of nanoseconds [30, 31, 36–38], which is in stark contrast to the observed short lifetimes observed in the Kerr rotation measurements on the one device that is showing the possible moiré features in its interlayer exciton emission (compare Figs. 1d and 1e in the main manuscript). Therefore, we conclude that our TRKR measurements are in all likelihood unable to directly detect these excitons, which is in accordance to sections 10 and 10 of

this Supplementary Information and the conclusion of the main manuscript that we primarily probe the valley polarization of free charge carriers.

Furthermore, the vast majority of studies examining the effects of a moiré potential in TMD-based heterobilayers have conducted their experiments on samples without a gate. Therefore, very little is known about the effects of a moiré potential when the Fermi level is tuned in either the conduction or valence band. However, it is at the band edges where we observe our most important finding, namely the interlayer transfer of a valley polarization from excitons to valley-polarized free charge carriers. Additionally, we note that all experiments on moiré excitons are performed with very low laser powers, usually in the lower μW range for cw experiments and even in the nW range for time-resolved PL measurements with pulse widths of at least tens of picoseconds. Instead, TRKR measurements are usually performed with pulse widths in the lower ps range (in our case about 3 ps) or even in the higher fs range with laser powers of up to hundreds of μW. Since laser spot sizes are quite comparable between most publications (around $1 - 10\,\mu$m FWHM), the total amount of photoexcited carriers is much higher in TRKR measurements compared to studies investigating moiré effects. However, a high density of photo-excited or gated-induced charge carriers can cause band renormalization effects [27, 39, 40]. Whether the energy scale of the moiré potential is actually relevant under such conditions must be the scope of further studies.

Supplementary Note 6: Additional data

Supplementary Figure 6 shows the Kerr rotation amplitude of the band-gap related signal in LTA device #1 when pumping at the trion energy of $MoSe_2$ and probing at the trion energy of WSe_2. Thus, it is the last of the four possible combinations of pump and probe energies, while the others are shown in Fig. 2 of the main manuscript. It was also the last energy combination that we measured, as the leakage current over the hBN gate dielectric dramatically increased during this measurement. To avoid a breakthrough of the gate dielectric that would made any further gate-dependent measurements impossible, we stopped the measurement at $V_{gate} = -3\,$V. However, up to this gate voltage the gate-dependence of the Kerr amplitude is in very good agreement to the one that is shown in Fig. 2d of the main manuscript, where the pump and probe energies are both set to the trion energy of WSe_2. This is in complete accordance to our model in Fig. 3 of the main manuscript as the energies of the bound exciton states in WSe_2 (dashed line in the band gap of Fig. 3h) are energetically lower than the bright intralayer exciton energies in $MoSe_2$ that are primarily excited by the pump pulse. Through scattering events the pump pulse can therefore occupy the bound excitons states in the band gap of WSe_2, creating the long-lived Kerr signal when the probe is set to the trion energy of WSe_2.

We note that in our study we show only the amplitudes and lifetimes of the Kerr signals that we attribute to either the long-lived bound exciton states or the valley polarization of free charge carriers. In several of our measurements we also observe a very short-lived signal with a lifetime of up to a few tens of picoseconds. Sometimes this signal is so short-lived that we can only observe it in the first two or three data points after zero delay, which is not enough for a reliable fit. We attribute this signal
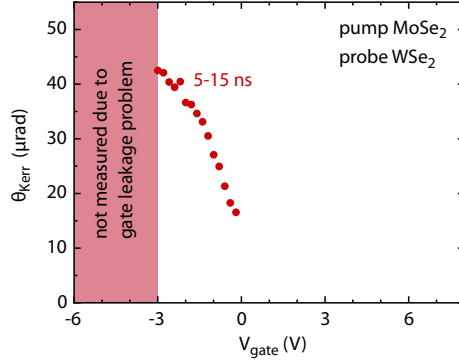
Supplementary Figure 6 Gate-dependent TRKR amplitude of the band-gap related signal in WSe$_2$ when the pump energy is set to the trion energy of MoSe$_2$ and the probe energy is set to the trion energy of WSe$_2$. The measurement was conducted at 10 K.

to a polarization of bright intralayer excitons before they scatter and recombine. As such a polarization of bright intralayer excitons is not the scope of our study, we have excluded the amplitudes and lifetimes of this signal (in case where we were actually able to fit them) from the figures in this study. The fact that no data points for gate voltage above $V_{\text{gate}} = 0$ V are presented in Fig. 2d of the main manuscript or Supplementary Figure 6 is due to the fact that no signal besides this very short-lived bright exciton signal is present in these gate voltage ranges.

Supplementary Note 7: Spatial positioning of the laser beams

For the TRKR measurements, we use a single lens to focus the two spatially separated pump and probe beams on the same spot of the device (see Fig. 10 in the Supplemental Material of Ref. [7]). The advantage of this approach is that the two beams can be separated quite easily after they have been reflected from the sample (see aforementioned figure in Ref. [7]). The disadvantage is that the minimum spot size is limited compared to the use of a microscope objective (the latter does not have a large enough entrance pupil diameter for two spatially separated laser beams). Using a single lens therefore limits the spot diameters to $6 - 8 \, \mu$m measured as the full width at half maximum (FWHM).

The TRKR data therefore probes an area of tens of μm^2. As typical dimensions of TMD-based heterobilayer devices are at most a few tens of micrometers in length, we therefore search for the one spot in our devices that is furthest away from edges, folds and bubbles in the heterostructure to diminish contributions from these features to the largest possible extent. All measurements (TRKR and PL) are subsequently conducted on this single spot.

Supplementary Note 8: Band alignment of LTA devices

As explained in the main manuscript, our PL measurements on the LTA devices reveal that the conduction band minima of $MoSe_2$ and WSe_2 seem to be aligned close to each other, most likely due to an n-doping of the constituent TMD layers. In the schematics of Fig. 3 of the main manuscript we draw the conduction band minimum of $MoSe_2$ slightly below the one of WSe_2. Our reason for this is that in the electron regime of LTA device #1 and #3 ($V_{gate} > 1\,V$ in Fig. 3 and $V_{gate} > 0\,V$ in Fig. 4 of the main manuscript), we do not observe a Kerr signal that we can attribute to a valley polarization of free charge carriers in WSe_2 if we probe at the trion energy of WSe_2 (see absent blue data points in Figs. 2d and 4b of the main manuscript). We therefore conclude that the conduction band minimum of $MoSe_2$ has to be slightly lower so that the polarized free charge carriers can occupy only these states, resulting in the Kerr rotation signal that we can attribute to the valley polarization of free charge carriers when probing at the trion energy of $MoSe_2$ (see blue data points in Figs. 2e and 4c in the main manuscript).

Supplementary References

[1] Malard, L.M., Alencar, T.V., Barboza, A.P.M., Mak, K.F., Paula, A.M.: Observation of intense second harmonic generation from MoS_2 atomic crystals. Phys. Rev. B **87**, 201401 (2013) https://doi.org/10.1103/PhysRevB.87.201401

[2] Li, Y., *et al.*: Probing Symmetry Properties of Few-Layer MoS_2 and h-BN by Optical Second-Harmonic Generation. Nano Lett. **13**(7), 3329–3333 (2013) https://doi.org/10.1021/nl401561r

[3] Hsu, W.T., *et al.*: Second harmonic generation from artificially stacked transition metal dichalcogenide twisted bilayers. ACS Nano **8**(3), 2951–2958 (2014) https://doi.org/10.1021/nn500228r

[4] Ersfeld, M., *et al.*: Unveiling Valley Lifetimes of Free Charge Carriers in Monolayer WSe_2. Nano Lett. **20**(5), 3147–3154 (2020) https://doi.org/10.1021/acs.nanolett.9b05138

[5] Wang, G., *et al.*: Colloquium: Excitons in atomically thin transition metal dichalcogenides. Rev. Mod. Phys. **90**, 021001 (2018) https://doi.org/10.1103/RevModPhys.90.021001

[6] Plechinger, G., *et al.*: Trion fine structure and coupled spin-valley dynamics in monolayer tungsten disulfide. Nat. Commun. **7**, 12715 (2016) https://doi.org/10.1038/ncomms12715

[7] Volmer, F., Pissinger, S., Ersfeld, M., Kuhlen, S., Stampfer, C., Beschoten, B.: Intervalley dark trion states with spin lifetimes of 150 ns in WSe_2. Phys. Rev. B

95, 235408 (2017) https://doi.org/10.1103/PhysRevB.95.235408

[8] Hunt, R.P.: Magneto-Optic Scattering from Thin Solid Films. J. Appl. Phys. **38**(4), 1652–1671 (1967) https://doi.org/10.1063/1.1709738

[9] Zak, J., Moog, E.R., Liu, C., Bader, S.D.: Universal approach to magneto-optics. J. Magn. Magn. Mater. **89**(1), 107–123 (1990) https://doi.org/10.1016/0304-8853(90)90713-Z

[10] You, C.-Y., Shin, S.-C.: Generalized analytic formulae for magneto-optical Kerr effects. J. Appl. Phys. **84**(1), 541–546 (1998) https://doi.org/10.1063/1.368058

[11] Jin, C., *et al.*: Identification of spin, valley and moiré quasi-angular momentum of interlayer excitons. Nat. Phys. **15**(11), 1140–1144 (2019) https://doi.org/10.1038/s41567-019-0631-4

[12] Wu, F., Lovorn, T., MacDonald, A.H.: Theory of optical absorption by interlayer excitons in transition metal dichalcogenide heterobilayers. Phys. Rev. B **97**, 035306 (2018) https://doi.org/10.1103/PhysRevB.97.035306

[13] Yu, H., Wang, Y., Tong, Q., Xu, X., Yao, W.: Anomalous Light Cones and Valley Optical Selection Rules of Interlayer Excitons in Twisted Heterobilayers. Phys. Rev. Lett. **115**, 187002 (2015) https://doi.org/10.1103/PhysRevLett.115.187002

[14] Yu, H., Liu, G.-B., Yao, W.: Brightened spin-triplet interlayer excitons and optical selection rules in van der Waals heterobilayers. 2D Mater. **5**(3), 035021 (2018) https://doi.org/10.1088/2053-1583/aac065

[15] Blaha, P., Schwarz, K., Tran, F., Laskowski, R., Madsen, G.K., Marks, L.D.: WIEN2k: An APW+lo program for calculating the properties of solids. J. Chem. Phys. **152**(7), 074101 (2020) https://doi.org/10.1063/1.5143061

[16] Perdew, J.P., Burke, K., Ernzerhof, M.: Generalized Gradient Approximation Made Simple. Phys. Rev. Lett. **77**, 3865–3868 (1996) https://doi.org/10.1103/PhysRevLett.77.3865

[17] Grimme, S., Antony, J., Ehrlich, S., Krieg, H.: A consistent and accurate ab initio parametrization of density functional dispersion correction (DFT-D) for the 94 elements H-Pu. J. Chem. Phys. **132**(15), 154104 (2010) https://doi.org/10.1063/1.3382344

[18] Singh, D.J., Nordstrom, L.: Planewaves, Pseudopotentials, and the LAPW Method. Springer, ??? (2006)

[19] Kormányos, A., *et al.*: k· p theory for two-dimensional transition metal dichalcogenide semiconductors. 2D Mater. **2**(2), 022001 (2015) https://doi.org/10.1088/2053-1583/2/2/022001

[20] Zollner, K., Faria Junior, P.E., Fabian, J.: Strain-tunable orbital, spin-orbit, and optical properties of monolayer transition-metal dichalcogenides. Phys. Rev. B **100**, 195126 (2019) https://doi.org/10.1103/PhysRevB.100.195126

[21] Faria Junior, P.E., Zollner, K., Woźniak, T., Kurpas, M., Gmitra, M., Fabian, J.: First-principles insights into the spin-valley physics of strained transition metal dichalcogenides monolayers. New J. Phys. **24**(8), 083004 (2022) https://doi.org/10.1088/1367-2630/ac7e21

[22] Kunstmann, J., *et al.*: Momentum-space indirect interlayer excitons in transition-metal dichalcogenide van der Waals heterostructures. Nat. Phys. **14**(8), 801–805 (2018) https://doi.org/10.1038/s41567-018-0123-y

[23] Faria Junior, P.E., Fabian, J.: Signatures of Electric Field and Layer Separation Effects on the Spin-Valley Physics of $MoSe_2$/WSe_2 Heterobilayers: From Energy Bands to Dipolar Excitons. Nanomater. **13**(7), 1187 (2023) https://doi.org/10.3390/nano13071187

[24] Zhang, F., Li, W., Dai, X.: Modulation of electronic structures of $MoSe_2$/WSe_2 van der Waals heterostructure by external electric field. Solid State Commun. **266**, 11–15 (2017) https://doi.org/10.1016/j.ssc.2017.08.010

[25] Huang, D., Kaxiras, E.: Electric field tuning of band offsets in transition metal dichalcogenides. Phys. Rev. B **94**, 241303 (2016) https://doi.org/10.1103/PhysRevB.94.241303

[26] Icking, E., et al.: Transport Spectroscopy of Ultraclean Tunable Band Gaps in Bilayer Graphene. Adv. Electron. Mater., 2200510 (2022) https://doi.org/10.1002/aelm.202200510

[27] Meng, Y., *et al.*: Electrical switching between exciton dissociation to exciton funneling in $MoSe_2$/WS_2 heterostructure. Nat. Commun. **11**(1), 2640 (2020) https://doi.org/10.1038/s41467-020-16419-x

[28] Steinhoff, A., Rösner, M., Jahnke, F., Wehling, T.O., Gies, C.: Influence of Excited Carriers on the Optical and Electronic Properties of MoS_2. Nano Lett. **14**(7), 3743–3748 (2014) https://doi.org/10.1021/nl500595u

[29] Erben, D., Steinhoff, A., Gies, C., Schönhoff, G., Wehling, T.O., Jahnke, F.: Excitation-induced transition to indirect band gaps in atomically thin transition-metal dichalcogenide semiconductors. Phys. Rev. B **98**(3), 035434 (2018) https://doi.org/10.1103/physrevb.98.035434

[30] Huang, D., Choi, J., Shih, C.-K., Li, X.: Excitons in semiconductor moiré superlattices. Nat. Nanotechnol. **17**(3), 227 (2022) https://doi.org/10.1038/s41565-021-01068-y

[31] Seyler, K.L., et al.: Signatures of moiré-trapped valley excitons in MoSe$_2$/WSe$_2$ heterobilayers. Nature **567**(7746), 66–70 https://doi.org/10.1038/s41586-019-0957-1

[32] Förg, M., et al.: Moiré excitons in MoSe$_2$-WSe$_2$ heterobilayers and heterotrilayers. Nat. Commun. **12**(1), 1656 https://doi.org/10.1038/s41467-021-21822-z

[33] Rosenberger, M.R., *et al.*: Twist Angle-Dependent Atomic Reconstruction and Moiré Patterns in Transition Metal Dichalcogenide Heterostructures. ACS Nano **14**(4), 4550–4558 (2020) https://doi.org/10.1021/acsnano.0c00088

[34] Zhao, S., et al.: Excitons in mesoscopically reconstructed moiré heterostructures. Nat. Nanotechnol. https://doi.org/10.1038/s41565-023-01356-9

[35] Brotons-Gisbert, M., *et al.*: Spin-layer locking of interlayer excitons trapped in moiré potentials. Nat. Mater. **19**(6), 630–636 (2020) https://doi.org/10.1038/s41563-020-0687-7

[36] Mahdikhanysarvejahany, F., et al.: Temperature dependent moiré trapping of interlayer excitons in MoSe$_2$-WSe$_2$ heterostructures. npj 2D Mater. Appl. **5**(1), 67 https://doi.org/10.1038/s41699-021-00248-7

[37] Shinokita, K., Watanabe, K., Taniguchi, T., Matsuda, K.: Valley Relaxation of the Moiré Excitons in a WSe$_2$/MoSe$_2$ Heterobilayer. ACS Nano **16**(10), 16862–16868 (2022) https://doi.org/10.1021/acsnano.2c06813

[38] Choi, J., *et al.*: Twist Angle-Dependent Interlayer Exciton Lifetimes in van der Waals Heterostructures. Phys. Rev. Lett. **126**, 047401 (2021) https://doi.org/10.1103/PhysRevLett.126.047401

[39] Chernikov, A., Ruppert, C., Hill, H.M., Rigosi, A.F., Heinz, T.F.: Population inversion and giant bandgap renormalization in atomically thin WS$_2$ layers. Nat. Photonics **9**(7), 466–470 (2015) https://doi.org/10.1038/nphoton.2015.104

[40] Cunningham, P.D., Hanbicki, A.T., McCreary, K.M., Jonker, B.T.: Photoinduced Bandgap Renormalization and Exciton Binding Energy Reduction in WS$_2$. ACS Nano **11**(12), 12601–12608 (2017) https://doi.org/10.1021/acsnano.7b06885